Journal of
Synchrotron
Radiation

ISSN 0909-0495

Received 11 March 2005
Accepted 8 July 2005

Grazing-incidence scattering of coherent X-rays from a liquid surface

Anders Madsen,[a]* Tilo Seydel,[b] Metin Tolan[c] and Gerhard Grübel[d]

[a]European Synchrotron Radiation Facility, BP 220, 38043 Grenoble, France, [b]Institut Laue–Langevin, BP 156, 38042 Grenoble, France, [c]Universität Dortmund, Exp. Physik 1, Otto-Hahn-Straße 4, 44221 Dortmund, Germany, and [d]HASYLAB at DESY, Notkestrasse 85, 22603 Hamburg, Germany. E-mail: amadsen@esrf.fr

The scattering image produced by coherent X-rays appears grainy and is denoted a speckle pattern. An analysis of the static and time-dependent properties of a speckle pattern generated by scattering of a partially coherent synchrotron beam from a liquid surface is given here. Unique surface sensitivity is achieved by applying the X-rays under a grazing angle of incidence. The observed contrast of the speckle pattern depends on the momentum transfer parallel to the surface, unlike the case of transmission small-angle X-ray scattering (SAXS), where essentially no q dependence of the contrast has been observed. The appearance of the speckles and the contrast of the image can be understood qualitatively by use of geometrical arguments and by the fact that liquid surfaces are extremely flat.

Keywords: coherent X-ray scattering; speckle patterns; liquid surfaces; X-ray photon correlation spectroscopy (XPCS).

1. Introduction

Scattering with partially coherent X-rays (Sinha *et al.*, 1998) has become possible since the advent of brilliant third-generation synchrotron sources based on undulator devices. Coherent scattering images from a disordered system display grainy features, known as speckles, due to interference between scattered waves with different phase shifts (Ludwig, 1988; Sutton *et al.*, 1991; Grübel & Abernathy, 1997; Abernathy *et al.*, 1998; Tsui *et al.*, 1998; Lumma *et al.*, 2000). Grazing-incidence surface scattering with coherent X-rays has previously been demonstrated experimentally (Cai *et al.*, 1994; Robinson *et al.*, 1995). Since the static speckle pattern reflects the exact spatial arrangement of the scattering object, the profile of the surface may be reconstructed by use of an inversion algorithm based on oversampling (Vartanyants *et al.*, 1997; Miao *et al.*, 1998; Robinson *et al.*, 1999).

In X-ray photon correlation spectroscopy (XPCS) (Mochrie *et al.*, 1997; Grübel *et al.*, 2000; Lurio *et al.*, 2000; Lumma *et al.*, 2001; Sikharulidze *et al.*, 2002; Kim *et al.*, 2003; Madsen *et al.*, 2003; Thurn-Albrecht *et al.*, 2003; Falus *et al.*, 2005; Robert *et al.*, 2005) the time variation of a speckle pattern is used to extract information about the dynamics of the sample by measuring the normalized intensity–intensity time-correlation function $G(\tau, q) = \langle I(t+\tau, q)I(t, q)\rangle / \langle I(t, q)\rangle^2$. Some years ago we demonstrated the possibility of detecting lateral capillary wave motion on a liquid glycerol surface by use of XPCS (Seydel *et al.*, 2001). In this case, the dynamic is characterized by a relaxation time τ_0, which can be determined by fitting $G(\tau, q)$ to an exponential decay,

$$G(\tau, q) = \beta \exp(-\tau/\tau_0) + 1, \quad (1)$$

where β is the q-dependent contrast or coherence factor. Glycerol is a prototypical glass former and the surface motion can be arrested by an adequate lowering of the temperature because the shear viscosity increases exponentially with decreasing temperature. This is used in the present experiment to measure a static speckle pattern from which the spatial intensity–intensity autocorrelation function can be calculated. Hence, for glycerol it is possible to perform a complete (spatial and temporal) analysis of the speckle pattern since one can change from dynamic to static speckles simply by lowering the temperature.

There are three main purposes of this article: (i) to discuss the one-dimensional character of the scattering image obtained from a liquid surface when it is illuminated by X-rays under grazing incidence, (ii) to discuss the static speckle pattern and analyze it in terms of the spatial autocorrelation function and (iii) to discuss the influence of the speckle image's one-dimensional character on the contrast of the time correlation function $G(\tau, q)$ obtained by XPCS and compare with the static speckle analysis.

2. The one-dimensional scattering image

Fig. 1 shows the scattering image from a glycerol surface produced by a partially coherent X-ray beam applied under

grazing angle incidence, $\theta_i = 0.08^\circ$ (Seydel *et al.*, 2003). The image was recorded by a direct illumination CCD camera with 22.5 µm pixel size. The experiment was performed at the ID10A Troïka I beamline at the European Synchrotron Radiation Facility (ESRF), where three undulators operating in series were set to have coinciding harmonics at 8 keV ($\lambda = 1.54$ Å). The emerging beam was diffracted horizontally from a single-bounce Si(111) Bragg monochromator crystal ($\Delta\lambda/\lambda \simeq 1.4 \times 10^{-4}$) and vertically from a Pt-coated glass mirror to obtain monochromatic radiation without contributions from higher-order harmonics. The source size (FWHM) was approximately 30 µm × 900 µm (v × h) and the source–sample distance was 46 m. In the vertical direction, the synchrotron beam was focused by a cylindrical compound refractive beryllium lens (Snigirev *et al.*, 1996) in order to symmetrize the transverse coherence lengths and enhance the flux. In the horizontal direction the beam was collimated to achieve a smaller source size. A 10 µm pinhole before the sample was used to select the 'coherent' part of the beam. The intensity was $\sim 2 \times 10^9$ photons s^{-1} through the pinhole. Right before the sample, a guard slit was carefully placed to block the fringes appearing from the pinhole scattering.

The beam was directed down towards the horizontal glycerol surface by a simultaneous tilt of the monochromator and rotation of the mirror. For glycerol, the critical angle α_c for total external reflection is $\sim 0.15^\circ$ at 8 keV. When X-rays are applied below the critical angle, an evanescent wave travels in the sample parallel to the surface with very limited penetration depth λ (Marra *et al.*, 1979; Vineyard, 1982), thus ensuring that the scattering observed is coming from the surface only. Therefore, $\theta_i = 0.08^\circ < \alpha_c$ was chosen.

The glycerol surface was prepared and stabilized in an evacuated sample cell with appropriate temperature control.

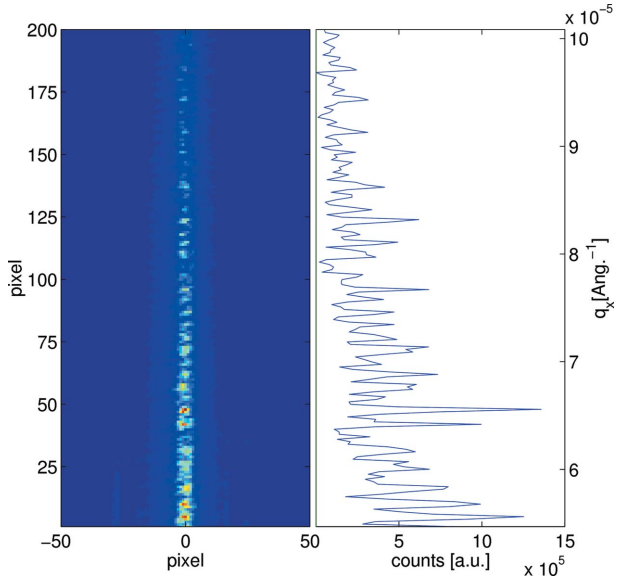

Figure 1
(Left) Static speckle pattern from a glycerol surface ($T = 193.0$ K) measured with a CCD camera. (Right) In-plane scattering profile corresponding to a central vertical section through the left image (Seydel *et al.*, 2003).

Details concerning the sample environment and sample preparation are given elsewhere (Seydel *et al.*, 2003). The scattering geometry is sketched in Fig. 2 and the area shown in Fig. 1 corresponds to a 200 pixel × 100 pixel $\simeq$ 4.4 mm × 2.2 mm section of the CCD chip located in the image plane. During the experiment, the glycerol surface was held at a constant temperature of $T = 193$ K. This is close to the glass transition temperature $T_G \simeq 186$ K, where the shear viscosity reaches 10^{12} Pa s, and therefore the surface motion due to capillary waves is very slow, on the time scale of many hours (Seydel *et al.*, 2001). The acquisition time of the image was approximately 1 h, during which the surface was static. From Fig. 1 it is evident that (i) the scattering profile is highly elongated along the q_x direction and (ii) the image appears grainy. These features will be explained below.

2.1. The scattering image in reciprocal space

To begin with we attempt to establish a simple picture of the scattering process and the interference phenomena involved. For this purpose we sketch in Fig. 2 a coherent X-ray beam, of

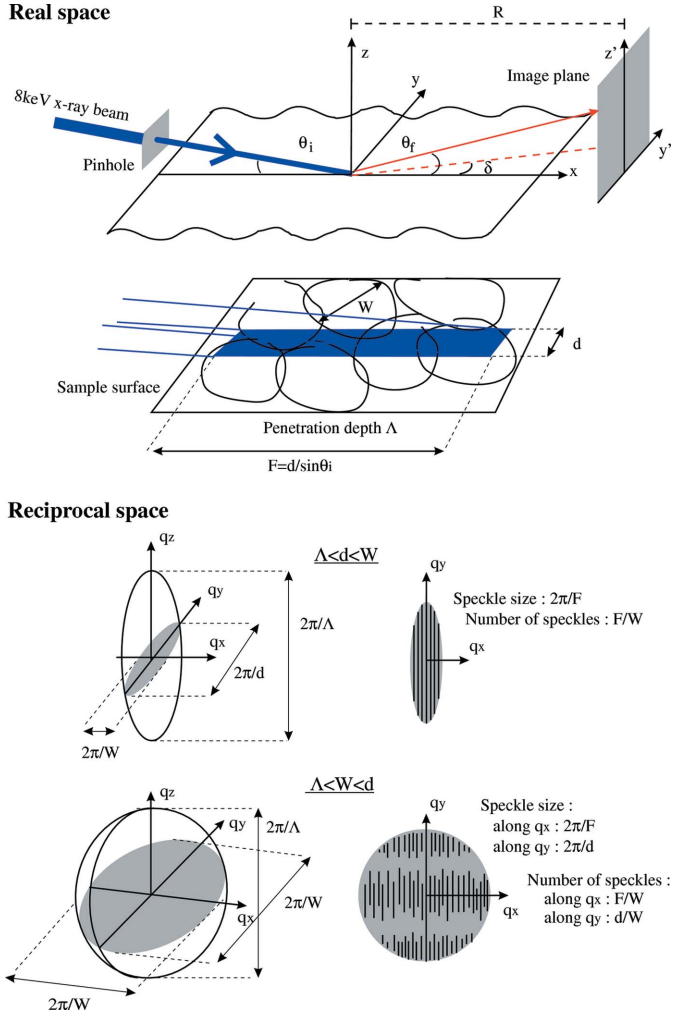

Figure 2
Sketch of the grazing-incidence scattering experiment in real and reciprocal space. The symbols in the figure are used throughout the text.

dimensions ($d \times d$) and wavelength λ, which is directed down towards a horizontal surface. In the following discussion the beam is considered to be fully coherent, but all arguments are still valid for a partially coherent beam with transverse coherence length d, although a lower speckle contrast is expected (see discussion later). The surface is assumed to consist of domains that modify the scattered field by different phase factors. At grazing incidence the footprint of the beam on the surface is highly elongated, and it is the scattering image appearing from this footprint that is sketched in reciprocal space in Fig. 2. The scattering volume in reciprocal space can be approximated by an ellipsoid with dimensions proportional to the inverse dimension of the coherently illuminated volume in real space. Therefore the scattering image will appear highly elongated along q_z as a result of the small penetration depth Λ of the beam when θ_i is smaller than the critical angle for total external reflection. Apart from Λ, there are three other dimensions of interest in real space, namely the beam size d, the domain size W, and the length of the footprint $F = d/\sin\theta_i$. We assume that $F \gg W$ and the discussion can be split into two cases: $d < W$ and $d > W$. Since $F \gg W$ the scattered wavefront is modified by different phase factors along the footprint (x direction) and therefore, in both cases, there will be an intensity modulation (speckle) in the q_x direction. This structure arises as a consequence of interference of partial waves scattered from the different domains. The speckle separation in reciprocal space is determined by $2\pi/(N_x W)$, where N_x is the number of domains illuminated by the beam in the x direction. In this case, it is identical to the width of one speckle, given as $2\pi/F$. If $d > W$ there will, in addition, be a speckle modulation along q_y, with a characteristic period of $2\pi/d$. According to the above discussion, the scattering volumes in reciprocal space are drawn in Fig. 2 as ellipsoids with internal speckle structure (Robinson *et al.*, 1995). The shape of an ellipsoid is highly elongated by a factor d/Λ, typically 1000, along the q_z direction. This is suppressed in the figure for clarity. In the q_z direction the ellipsoid is featureless (no speckles) as $q_z < 2\pi/\Lambda$ because of the small value of Λ. The ellipsoid dimension along q_x is $2\pi/W$, whereas along q_y it is either $2\pi/d$ or $2\pi/W$ for the two cases $d < W$ and $d > W$, respectively. From Fig. 2 we predict that along q_y a speckle structure will only appear as a consequence of surface disorder when $W < d$. In other words, disorder on small lateral length scales generates speckles along q_y, while disorder on larger length scales results in speckles along q_x. This statement is in good agreement with the observation that speckles are confined to the q_x axis in Fig. 1, which shows the speckle pattern from an almost perfectly flat surface [r.m.s. roughness < 3Å (Seydel *et al.*, 2002)] with large correlation lengths parallel to the surface.

2.2. The scattering image in real space

To simulate the speckle pattern in the image plane, a conversion between reciprocal space q coordinates and real space image plane coordinates is required. A coordinate in the image plane is defined by the take-off angle θ_f between the scattered beam and the surface, and the angle δ between the scattered beam and the specular scattering plane (see Fig. 2). The components of the momentum transfer are given as

$$\mathbf{q} = \begin{pmatrix} q_x \\ q_y \\ q_z \end{pmatrix} = \frac{2\pi}{\lambda} \begin{pmatrix} \cos\theta_i - \cos\theta_f \cos\delta \\ \cos\theta_f \sin\delta \\ -(\sin\theta_i + \sin\theta_f) \end{pmatrix}. \quad (2)$$

By differentiating the above and using the approximation $\delta \simeq 0$, which applies near the specular scattering plane, we obtain for $\Delta\delta$

$$|\Delta q_x| = (2\pi/\lambda)|\Delta\delta| \sin\delta \cos\theta_f \simeq 0, \quad (3)$$

$$|\Delta q_y| = (2\pi/\lambda)|\Delta\delta| \cos\theta_f \cos\delta \simeq (2\pi/\lambda)|\Delta\delta| \cos\theta_f, \quad (4)$$

and for $\Delta\theta_f$

$$|\Delta q_x| = (2\pi/\lambda)|\Delta\theta_f| \sin\theta_f \cos\delta \simeq (2\pi/\lambda)|\Delta\theta_f| \sin\theta_f, \quad (5)$$

$$|\Delta q_y| = (2\pi/\lambda)|\Delta\theta_f| \sin\theta_f \sin\delta \simeq 0. \quad (6)$$

The interpretation of the above is straightforward: q_y and q_x vary with δ and θ_f, respectively. Equation (5) together with the relation for the speckle width in reciprocal space $|\Delta q_x| = 2\pi/F$ yield for the angular speckle width

$$|\Delta\theta_f| \simeq (\lambda/d)(\sin\theta_i/\sin\theta_f). \quad (7)$$

It is important to notice that in the limit $\theta_i = 90°$, $\theta_f = -90°$, equation (7) reduces to the well known approximation $|\Delta\theta_f| \simeq \lambda/d$, valid for the speckle size in small-angle X-ray scattering (SAXS) transmission geometry. Also note that in the specular case, *i.e.* when $\theta_i = \theta_f$, equation (7) reduces to the above-mentioned SAXS result as expected, since the surface then acts like a simple mirror. The axes of the image plane are denoted $y' (= R\tan\delta)$ and $z' (= R\tan\theta_f)$ (Fig. 2), and in the small θ_f limit we find for the real space speckle size

$$|\Delta z'| \simeq (\lambda R/d)(\sin\theta_i/\sin\theta_f). \quad (8)$$

This means that the speckles width is decreasing as θ_f increases so the speckle image is gradually compressed along the z' axis with increasing z'. Along the y' axis, the speckle image is not compressed according to equation (4), but in this direction there are only few speckles visible when the sample surface is almost perfectly flat and $\theta_i < \alpha_c$ (see Fig. 1). In addition, one notes that equation (8) predicts the speckles to be elongated in the q_x direction (*i.e.* larger than $\lambda R/d$) if $\theta_f < \theta_i$, *i.e.* in a grazing exit scattering geometry (Pfeiffer *et al.*, 2004).

2.3. Numerical simulation

A numerical simulation of coherent scattering from a liquid surface was carried out to verify the analysis presented above. In the case of a liquid, the surface does not have real domains, as sketched in Fig. 2, but the surface is covered by thermally excited capillary waves. Hence, a liquid surface can be thought of as a random landscape of peaks and valleys characterized by a function $h(x, y)$, giving the surface height at each point (x, y). A lateral correlation length (or domain size W) is equivalent to the distance over which $h(x, y)$ remains corre-

lated. Usually the height–height correlation function is defined as $g(R) = g(\delta x, \delta y) = \langle [h(x_0, y_0) - h(x, y)]^2 \rangle$, where the average is taken over all points of the surface (x, y) with $|x_0 - x| = \delta x$ and $|y_0 - y| = \delta y$. Here $R = [(\delta x)^2 + (\delta y)^2]^{1/2}$ and for a perfectly flat surface $g(R) = 0$. For a liquid surface one finds $g(R) \propto \sigma_h^2 \ln(R)$, where σ_h is denoted the r.m.s. roughness caused by the thermally excited capillary waves (Sinha *et al.*, 1988). We approximate a liquid surface covered with 'frozen-in' over-damped capillary waves by an xy plane with randomly centered Gaussian-shaped height distortions. This is known to be a good approximation for the surface excitations when over-damped waves are concerned (Philips, 2004) and gives approximately the right functional form of $g(R)$. The intensity scattered from such a surface can be calculated for different exit angles θ_f, as shown in Fig. 3. The calculation is made for every point (y', z') in the image plane by integrating the scattered field amplitude from the surface and finding the intensity as

$$I(y', z') = \left| \int_{-F/2}^{F/2} \int_{-d/2}^{d/2} A \exp[i(2\pi/\lambda) D(R, x, y, y', z')] \times \alpha(x, y, \theta_i, \theta_f)\, \mathrm{d}x\, \mathrm{d}y \right|^2. \quad (9)$$

In practice, the above integration is performed numerically by summing the amplitudes from many discrete points on the surface, and a Monte Carlo procedure was used to select the points randomly in order to minimize resolution-induced artifacts in the simulation. A is the amplitude of the incident field, and we assume it to be constant and normalized according to

$$\int_{-F/2}^{F/2} \int_{-d/2}^{d/2} |A|^2\, \mathrm{d}x\, \mathrm{d}y = 1. \quad (10)$$

In equation (9), $D(R, x, y, y', z')$ is the distance from the point (x, y) on the surface to the point (y', z') in the image plane, with R as the sample–image plane distance (see Fig. 2). α is the phase shift due to the rough surface and is approximated by

$$\alpha(x, y, \theta_i, \theta_f) = \exp[i\,(2\pi/\lambda)\, h(x, y)\, (\sin\theta_i + \sin\theta_f)], \quad (11)$$

where $h(x, y)$ is the height of the surface at the point (x, y). The numerical simulation in Fig. 3 verifies the simple analysis summarized in Fig. 2. The result shown in Fig. 3 was obtained with $\sigma_h \simeq 3$ Å, and the speckles are confined to the z' axis of the image plane. The FWHM of one speckle is approximately $|\Delta q_x| \simeq 3 \times 10^{-7}$ Å^{-1}, in reasonable agreement with the estimate $2\pi/F$. Fig. 3 resembles the CCD image in Fig. 1 very much but is more regular, as a result of the simplicity of the liquid surface model used in the numerical simulation. The absolute intensities of the speckles in Fig. 3 are largely determined by the simulation procedure. This fact makes a more rigorous comparison between the two images in Figs. 1 and 3 difficult, but such a comparison is difficult anyway because of the limited resolution (22 µm pixel size) of the CCD.

In Fig. 4, the simulation in Fig. 3 was repeated with an increased roughness ($\sigma_h = 300$ Å). Therefore, $g(R)$ is increased and hence the lateral correlation length of the surface is reduced. As predicted, this gives rise to structure along q_y, which shows up in the image plane as speckles appearing off the z' axis (Fig. 4). We conclude that a high surface roughness effectively decreases the lateral correlation length and that this effect introduces speckles along q_y (Fig. 4), which are not present in the case of almost perfectly flat liquid surfaces (Fig. 3).

2.4. Contrast analysis of the static speckle pattern

The static speckle pattern in Fig. 1 can be characterized in terms of the contrast or the complex degree of coherence. In this section we calculate the complex degree of coherence $\mu(\mathbf{r}_1, \mathbf{r}_2)$ between two points $\mathbf{r}_1$ and $\mathbf{r}_2$ in the image plane, where $|\mu(\mathbf{r}_1, \mathbf{r}_2)|^2$ is equal to the normalized two-point intensity correlation function. The contrast is then given as $\beta = |\mu(\mathbf{r}_1 = \mathbf{r}_2)|^2$ (Born & Wolf, 1959) and the width of μ is a measure of the speckle width. The ensemble averaging due to the detector resolution can be accounted for by replacing $|\mu(\mathbf{r}_1, \mathbf{r}_2)|^2$ with the convolution

$$|\mu(\mathbf{r}_1, \mathbf{r}_2)|_C^2 = \iint S(\mathbf{r}_1 - \mathbf{r}') S(\mathbf{r}_2 - \mathbf{r}'') |\mu(\mathbf{r}_1, \mathbf{r}_2)|^2\, \mathrm{d}\mathbf{r}'\, \mathrm{d}\mathbf{r}'', \quad (12)$$

where S is a Gaussian resolution function (Abernathy *et al.*, 1998). The complex degree of coherence is defined as

$$\mu(\mathbf{r}_1, \mathbf{r}_2) = \int_V |A|^2 \exp\{i[\mathbf{q}(\mathbf{r}_1) - \mathbf{q}(\mathbf{r}_2)] \cdot v\}\, \mathrm{d}v, \quad (13)$$

where the integration is carried out over the whole sample volume V illuminated by the beam (Abernathy *et al.*, 1998). Here A is the normalized incident amplitude with

$$\int |A(v)|^2\, \mathrm{d}v = 1. \quad (14)$$

Using the image plane vector representation

$$\mathbf{r}_1 = \begin{pmatrix} 0 \\ y' \\ z' \end{pmatrix}, \quad \mathbf{r}_2 = \begin{pmatrix} 0 \\ y'' \\ z'' \end{pmatrix}, \quad (15)$$

the evaluation of $\mathbf{q}(\mathbf{r}_1) - \mathbf{q}(\mathbf{r}_2)$ yields

$$\mathbf{q}(\mathbf{r}_1) - \mathbf{q}(\mathbf{r}_2) = \frac{2\pi}{\lambda} \begin{pmatrix} \frac{R^2}{(R^2+z''^2)^{1/2}} \frac{1}{(R^2+y''^2)^{1/2}} - \frac{R^2}{(R^2+z'^2)^{1/2}} \frac{1}{(R^2+y'^2)^{1/2}} \\ \frac{Ry'}{(R^2+z'^2)^{1/2}(R^2+y'^2)^{1/2}} - \frac{Ry''}{(R^2+z''^2)^{1/2}(R^2+y''^2)^{1/2}} \\ \frac{z''}{(R^2+z''^2)^{1/2}} - \frac{z'}{(R^2+z'^2)^{1/2}} \end{pmatrix} = \begin{pmatrix} K_x \\ K_y \\ K_z \end{pmatrix}, \quad (16)$$

where R is the distance from the sample to the image plane, and thus the integral in equation (13) can be calculated. We find that the complex degree of coherence can be expressed as a product of three parameters:

$$\mu(\mathbf{r}_1, \mathbf{r}_2) = I_x \times I_y \times I_z, \quad (17)$$

with

$$I_x = \frac{1}{F}\int_{-F/2}^{F/2} \exp(iK_x x)\,\mathrm{d}x = \frac{2}{K_x F}\sin\left(\frac{K_x F}{2}\right), \tag{18}$$

$$I_y = \frac{1}{d}\int_{-d/2}^{d/2} \exp(iK_y y)\,\mathrm{d}y = \frac{2}{K_y d}\sin\left(\frac{K_y d}{2}\right) \tag{19}$$

$$I_z = \frac{1}{\Lambda}\int_{-\Lambda}^{0} \exp(iK_z z)\,\mathrm{d}z = \frac{1}{K_z \Lambda}\left\{\sin(K_z\Lambda) + i\left[\cos(K_z\Lambda) - 1\right]\right\}. \tag{20}$$

Owing to the very small penetration depth of the evanescent wave ($\Lambda \simeq 80$ Å for glycerol at 8 keV) when the X-ray beam is incident below the critical angle, I_z is a very slowly varying function close to unity, and thus in the following the approximation $I_z = 1$ is used. This approximation removes any influence of the probed depth of the sample, which in SAXS geometry is equivalent to the sample thickness, and marks an important difference between the present GISAXS case and the SAXS result, where the sample thickness plays an important role in limiting the contrast (Abernathy *et al.*, 1998; Tsui *et al.*, 1998; Lumma *et al.*, 2000).

$|\mu(\mathbf{r}_1, \mathbf{r}_2)|^2$ can now be calculated following equation (17), and the results are shown in Figs. 5 and 6, where the centers of

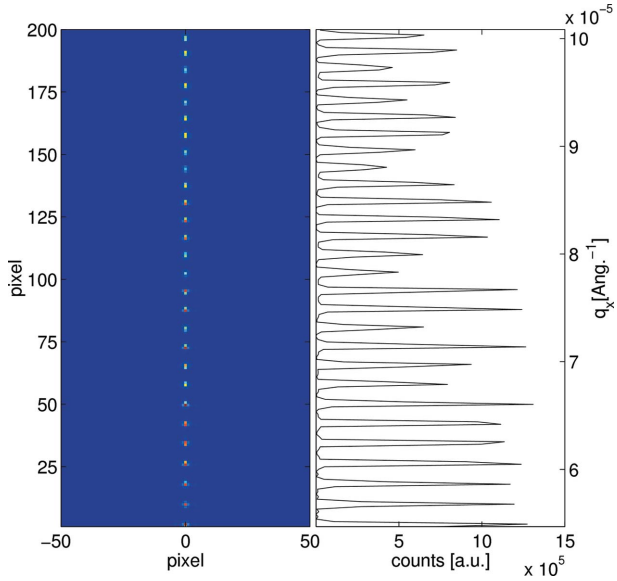

Figure 3
(Left) Calculated scattering image as described in the text with $R = 2.38$ m, $\theta_i = 0.08^\circ$ and $\sigma_h \simeq 3$ Å. (Right) In-plane scattering profile. The image center corresponds to $\theta_f = 0.37^\circ$ ($q_x = 7.74 \times 10^{-5}$ Å^{-1}), as in Fig. 1.

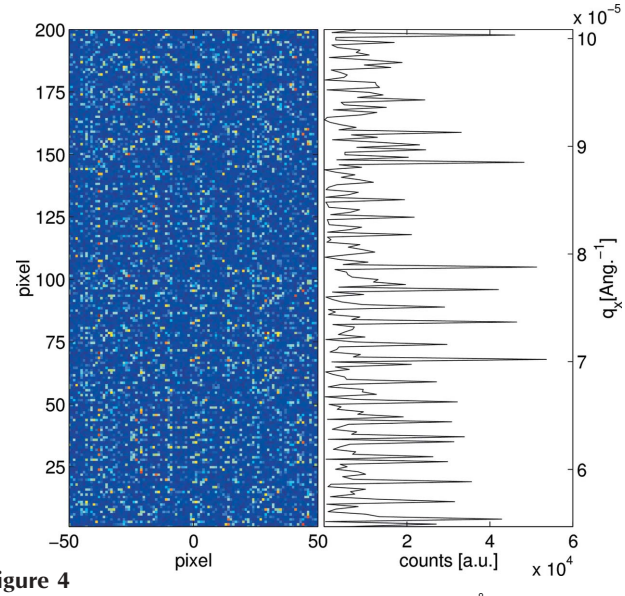

Figure 4
The same simulation as in Fig. 3 but with $\sigma_h = 300$ Å. The disorder on small length scales gives rise to speckle structure in the q_y direction.

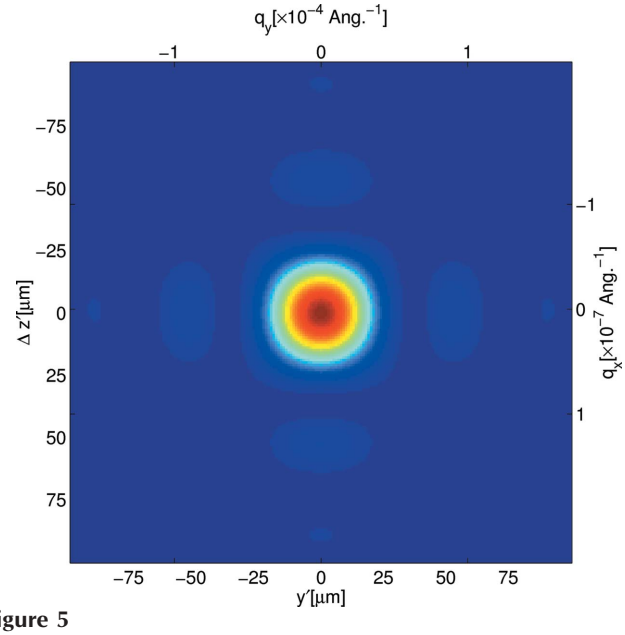

Figure 5
Complex degree of coherence calculated from the model described in the text with $\theta_i = 0.08^\circ$. The image shows the specular case $\theta_i = \theta_f$.

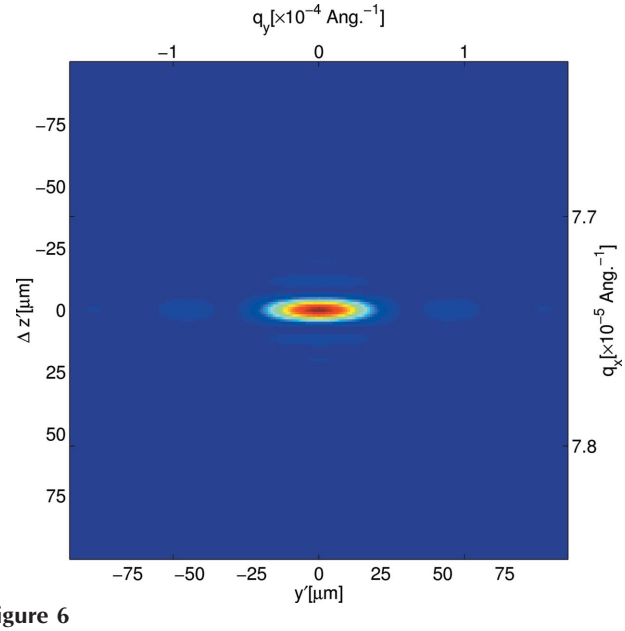

Figure 6
Complex degree of coherence calculated from the model described in the text with $\theta_i = 0.08^\circ$. The image center corresponds to $q_x = 7.74 \times 10^{-5}$ Å^{-1}, as in Figs. 1 and 3.

the images correspond to $(\theta_f, \delta) = (0.08, 0)$ and $(0.37, 0)^\circ$, respectively. The difference between Figs. 5 and 6 is solely in the z' direction, where the width of the central peak (the speckle width) changes. This difference illustrates the compression of the speckle pattern discussed previously and expressed in equations (7) and (8). $|\mu(\mathbf{r}_1, \mathbf{r}_2)|^2$, shown in Figs. 5 and 6, is equivalent to the Fraunhofer diffraction from a source with the dimensions of the footprint as seen from an exit angle θ_f, also known as the van Cittert-Zernike theorem (Born & Wolf, 1959). The peak values at $\mathbf{r}_1 = \mathbf{r}_2$ at the centers of Figs. 5 and 6 are the same, namely 1, thus indicating 100% contrast.

Obviously this is not correct and the double convolution in equation (12) expressing the ensemble averaging defined by the detector resolution must be incorporated. The double convolution with a Gaussian resolution function S of variance σ_S^2 [FWHM $l = \sigma_S(8\ln 2)^{1/2}$] can be performed in the y' (horizontal) and z' (vertical) directions of the image plane. If we let $\sigma_\mu(8\ln 2)^{1/2}$ denote the FWHM of the central peak ($\mathbf{r}_1 = \mathbf{r}_2$) of $|\mu(\mathbf{r}_1, \mathbf{r}_2)|^2$ in the y' direction (the speckle width), we find for the peak value β of $|\mu(\mathbf{r}_1 = \mathbf{r}_2)|^2_C$, the resolution convoluted degree of coherence,

$$\beta = \sigma_\mu\left[(\sigma_\mu)^2 + 2(\sigma_S)^2\right]^{-1/2} \tag{21}$$

and a similar expression in the z' direction. The above expression is based on the assumption that the detector resolution can be approximated by a Gaussian with variance σ_S^2. This is a good approximation when the peak value β is considered, and thus we will use equation (21) to calculate the contrast β and compare with the experimental data.

A contrast analysis was performed on the static speckle pattern in Fig. 1, for which the background (CCD dark-current and read-out noise) had been carefully subtracted and a flat-field correction applied. Non-overlapping areas of 1 pixel × 7 pixel corresponding to 22 µm × 154 µm were chosen, centered at increasing q_x, and the pixel–pixel contrast was determined by calculating

$$\beta(\mathbf{r}) = [\langle I(\mathbf{r})I(\mathbf{r})\rangle / \langle I(\mathbf{r})\rangle\langle I(\mathbf{r})\rangle] - 1. \tag{22}$$

The brackets $\langle\rangle$ denote averaging over the chosen area. The result is shown in Fig. 7, together with a model calculation based on equation (21), where a Gaussian function (FWHM 22 µm equal to the CCD pixel size) was used to describe the resolution of the CCD. The agreement between model and experiment in Fig. 7 is good and a decreasing contrast with increasing q_x can be observed. This trend is caused by the decrease in speckle width with increasing q_x that effectively increases the influence of the detector-averaging and thus decreases the contrast. The experimental points in Fig. 7 are quite scattered as a result of the averaging in equation (22) being performed over a small area, and because of a resolution problem (the speckle size and the pixel size of the CCD are almost identical). In general the data points in Fig. 7 seem to lie slightly below the model prediction, and this is not surprising since we use an ideal model assuming a fully coherent incident beam.

3. The dynamic speckle pattern

Using the experimental setup sketched in Fig. 2, a new CCD image shown in Fig. 8 was taken, this time with a glycerol temperature of $T = 238.7$ K. The speckle features that were so pronounced in Fig. 1 are now almost gone because the surface motion is much faster than the time it takes to acquire the image (∼60 min). Therefore, the scattered intensity is effectively averaged over all possible surface configurations, and thus the image in Fig. 8 resembles what would be obtained by applying a non-coherent X-ray beam.

With X-ray photon correlation spectroscopy (XPCS), the time structure of such a dynamic speckle pattern is analyzed and for this purpose the temporal intensity autocorrelation function $G(\tau, q)$ can be calculated [see equation (1)]. The contrast β of $G(\tau, q)$ is defined as $\beta(q) = G(\tau \rightarrow 0, q) - 1$ and is identical to the contrast previously calculated for the spatial autocorrelation function of the static speckle pattern.

3.1. XPCS experiment

The scattering geometry was the same as that used to record the CCD images (Figs. 1 and 8), but now the scattered radiation was measured by a point detector defined by a set of slits that could be operated independently in the horizontal and vertical directions. The detector–sample distance was $R = 2.38$ m, as previously, and the correlation function $G(\tau, q_x)$ was calculated by feeding the detector signal into an autocorrelator device that calculated G on-line. q_x denotes the momentum transfer parallel to the surface in the scattering plane and can be calculated from equation (2) with $\delta = 0^\circ$ and $\theta_i = 0.08^\circ$. An intensity autocorrelation function taken at $q_x = 7 \times 10^{-6}$ Å^{-1} is shown in Fig. 9(*a*). The correlation function from the incident beam (monitor) shows no features, but for the scattered beam (detector) it has the simple exponential shape of equation (1).

This result indicates that the surface dynamics is governed by over-damped capillary wave motion (Madsen *et al.*, 2004; Seydel *et al.*, 2001). The solid line in Fig. 9 is the best fit of equation (1) to the data, and a relaxation time τ_0 (3.65 ms) and contrast (61.5%) can be determined. The high value for the contrast indicates that the detection is homodyne, contrary to other studies where heterodyne mixing has been observed (Gutt *et al.*, 2003; Sikharulidze *et al.*, 2005; de Jeu *et al.*, 2005). In Fig. 9(*b*), correlation functions taken at different values of θ_f are shown. The pre-detector slit was kept constant, and the trend of decreasing contrast for increasing values of θ_f that can be observed in the figure is a clear indication of the decreasing speckle size. When the speckles get smaller the number of speckles registered by the detector through a given slit aperture increases, and so the contrast of the correlation function will decrease. A systematic study of the contrast variation as a function of vertical and horizontal detector slit opening was performed at fixed $q_x = 1.1 \times 10^{-5}$ Å^{-1}, corresponding to $\theta_f = 0.15^\circ$ with a glycerol temperature of $T = 265.5$ K. In order to compare with theory, the complex degree of coherence $|\mu(\mathbf{r}_1, \mathbf{r}_2)|^2$ was evaluated at the given q_x, and the FWHM of the central peak at $\mathbf{r}_1 = \mathbf{r}_2$ was determined. Finally, equa-

tion (21) was used to incorporate the effect of the different detector slit openings, and in Fig. 10 the result is plotted together with values of the contrast obtained by XPCS. The features of Fig. 10 are as expected from the analysis of the static speckle image; opening the slit in the vertical direction causes the contrast to drop faster than for a horizontal opening. This difference is due to the anisotropy of the speckle pattern discussed previously, and in this case the speckle size is larger in the horizontal than in the vertical direction by a factor $\sin\theta_f/\sin\theta_i = \sin 0.15^\circ/\sin 0.08^\circ \simeq 2$. At a certain horizontal opening, the measured contrast does not drop any more but stays constant, as indicated by the dashed line in Fig. 10; this effect was tested up to a horizontal slit opening of $l = 3000$ µm. This effect is due to the fact that there is no more scattered intensity to average over in this direction (see Figs. 1 and 8), *i.e.* the limit of the scattered intensity volume in reciprocal space has been reached. This situation was also indi-

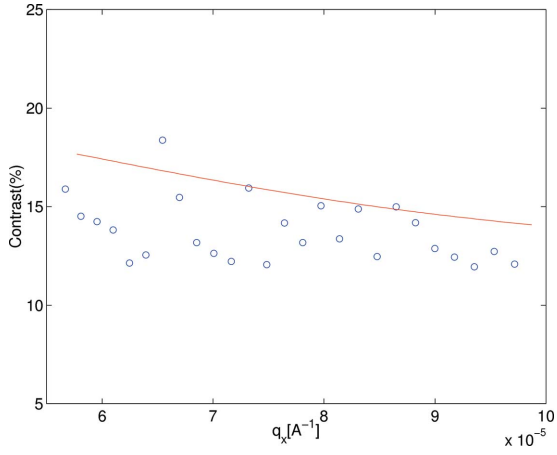

Figure 7
Contrast *versus* q_x calculated from the model (red line) and determined from the static speckles of Fig. 1 (blue circles) as described in the text.

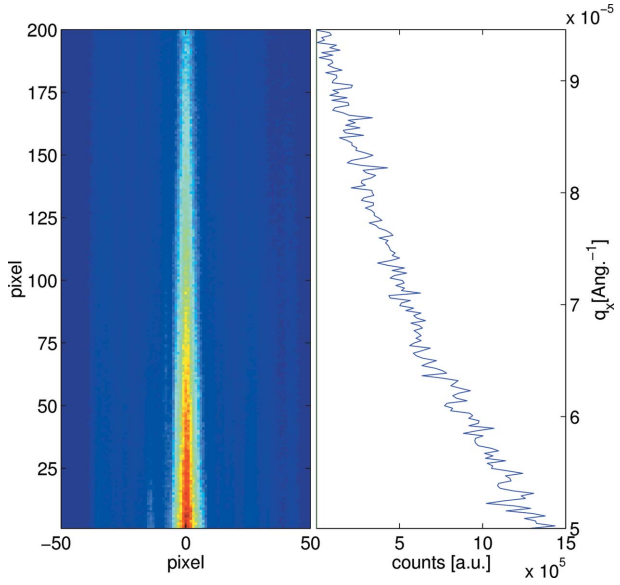

Figure 8
CCD image taken under conditions identical to those used for the image shown in Fig. 1 but with $T = 238.7$ K (Seydel *et al.*, 2003).

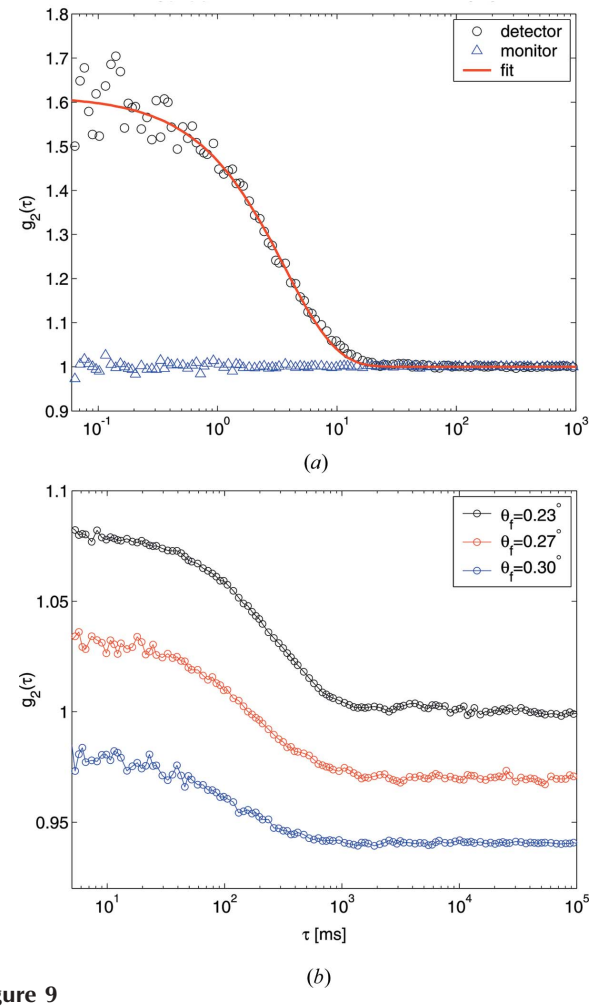

Figure 9
(*a*) Temporal intensity–intensity autocorrelation function measured in the experiment ($T = 265.5$ K, $q_x = 7 \times 10^{-6}$ Å^{-1}) with 15 µm × 15 µm detector slit. (*b*) Three correlation functions taken at $T = 234$ K at increasing θ_f values corresponding to $q_x = 2.9$, 4.1 and 5.2×10^{-5} Å^{-1}. The two latter curves have been shifted along the ordinate for clarity. The pre-detector slit was kept constantly at 100 µm × 100 µm and a decreasing contrast is obvious for increasing θ_f.

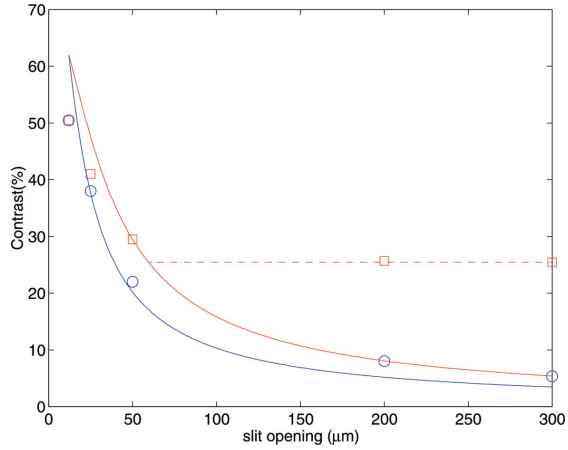

Figure 10
Contrast variation *versus* slit opening at $T = 265.5$ K and $\theta_f = 0.15^\circ$ ($q_x = 1.1 \times 10^{-5}$ Å^{-1}). Symbols are contrast values extracted from XPCS data and the solid lines are model calculations. Red squares and upper line: horizontal opening. Blue circles and lower line: vertical opening. The dashed line is explained in the text.

cated in Fig. 2, as the shaded regions in the $q_x q_y$ plane in reciprocal space.

In Fig. 2 this cutoff along q_y was explained either by the size of the beam d or by surface domains, depending on the magnitude of the domain size W with respect to d. As stated earlier, real domains do not exist on a simple liquid surface, but we have previously shown that increasing the surface roughness has the same effect as decreasing W (Figs. 3 and 4). At some point, when the roughness is increased, W gets smaller than d and then the cutoff along q_y is defined by W (see Fig. 2). Alternatively, the beam size d can explain the cutoff, and from equation (4) we estimate that this cross-over will happen at a slit opening of about 35 µm in our experiment. This is about half the cutoff value estimated from the intersection of the dashed line and the upper solid line in Fig. 10, and so we conclude that at $T = 265.5$ K the r.m.s. roughness [measured by X-ray reflectivity (Seydel *et al.*, 2002) to about 3Å] of the highly viscous glycerol surface implies a lateral surface correlation length of approximately half the beam size, *i.e.* about 5 µm.

4. Conclusion

In summary, we have determined the contrast of speckle patterns generated by a coherent X-ray beam scattered from a simple liquid surface under grazing angle incidence conditions. We show that the speckle pattern is highly anisotropic as a result of the grazing-incidence geometry, with a huge footprint on the sample. We demonstrate that the speckle size along q_x decreases with increasing q_x in GISAXS scattering geometry. This trend marks an important difference from transmission SAXS, where the speckle size is almost constant. In GISAXS we retrieve this result along the q_y direction, where only a small ($\propto \cos\delta$) dependence of contrast on q_y is found. Another difference between the GISAXS and the SAXS result is that the thickness of the sample does not play any role in GISAXS [equation (20), $I_z \simeq 1$], which is probably responsible for the huge contrast observed in some cases (Fig. 9*a*).

A basic calculation of the complex degree of coherence has been used to model both the contrast of the spatial correlation function (static case) and the time correlation function (dynamic case). The analysis yields good agreement between experiment and model (Figs. 7 and 10) and demonstrates the possibility of performing a complete analysis of the speckle pattern generated by coherent X-rays scattered from a surface. In the case of visible light, coherent laser sources have been available for many years, and here static speckle analysis is already an established technique used in detailed studies of surface morphology (Goodman, 1984; Lehmann, 1999).

In the future it is expected that grazing-incidence XPCS will move towards the study of nanostructured surfaces (solid or soft matter), where the surface sensitivity of X-rays combined with the possibility of probing slow dynamics at nanometre length scales is unique. Systems of interest include, for instance, self-assembled soft matter, glassy materials and hard-condensed matter surfaces exhibiting critical dynamics. For all future XPCS studies, however, it is the coherent flux together with the detector specifications that will set the limits for the accessible regions of time and space. In addition, the present work shows that geometrical effects may also play an important role when measuring spatial or temporal correlation functions and hence that this aspect should always be considered.

The simple model we use to describe the data in Fig. 10 fits quite well, but the point for the smallest slit opening (12 µm) lies ∼18% below the calculated curve. This result shows the limitations of the model, where losses in contrast due to the sample, finite source size and finite wavelength spread are not taken into account. Even if all of these factors do not contribute significantly, an 18% loss in contrast due to optical components of the beamline is not much and the results clearly indicate a major improvement compared with an earlier study (Abernathy *et al.*, 1998). An 18% loss in contrast indicates that more than 90% of the photons registered by the detector are participating in the coherent scattering. This limit is probably close to what one can reach in practice with third-generation synchrotron radiation, where the source is chaotic and therefore incoherent by nature (Lengeler, 2001).

The staff at the Troïka beamline are acknowledged for their assistance with the experiments. The work was partly supported by the projects Pr325/9-1,2,3 of the Deutsche Forschungsgemeinschaft.

References

Abernathy, D. L., Grübel, G., Brauer, S., McNulty, I., Stephenson, G. B., Mochrie, S. G. J., Sandy, A. R., Mulders, N. & Sutton, M. (1998). *J. Synchrotron Rad.* **5**, 37–47.
Born, M. & Wolf, E. (1959). *Principles of Optics.* New York: Pergamon Press.
Cai, Z. H., Lai, Z. H., Yun, W. B., McNulty, I., Huang, K. G. & Russel, T. P. (1994). *Phys. Rev. Lett.* **73**, 82–85.
Falus, P., Borthwick, M. A. & Mochrie, S. G. J. (2005). *Phys. Rev. Lett.* **94**, 016105.
Goodman, J. W. (1984). *Laser Speckle and Related Phenomena*, edited by J. C. Dainty, p. 39. Berlin: Springer-Verlag.
Grübel, G. & Abernathy, D. L. (1997). *Proc. SPIE*, **3154**, 103–109.
Grübel, G., Abernathy, D. L., Riese, D. O., Vos, W. L. & Wegdam, G. H. (2000). *J. Appl. Cryst.* **33**, 424–427.
Gutt, C., Ghaderi, T., Chamard, V., Madsen, A., Seydel, T., Tolan, M., Sprung, M., Grübel, G. & Sinha, S. K. (2003). *Phys. Rev. Lett.* **91**, 076104, 179903(E).
Jeu, W. H. de, Madsen, A., Sikharulidze, I. & Sprunt, S. (2005). *Physica B*, **357**, 39–44.
Kim, H. J., Rühm, A., Lurio, L. B., Basu, J., Lal, J., Lumma, D., Mochrie, S. G. J. & Sinha, S. K. (2003). *Phys. Rev. Lett.* **90**, 068302.
Lehmann, P. (1999). *Appl. Opt.* **38**, 1144–1152.
Lengeler, B. (2001). *Naturwissenschaften*, **88**, 249–260.
Ludwig, K. F. Jr (1988). *Phys. Rev. Lett.* **61**, 1526.
Lumma, D., Borthwick, M. A., Falus, P., Lurio, L. B. & Mochrie, S. G. J. (2001). *Phys. Rev. Lett.* **86**, 2042–2045.
Lumma, D., Lurio, L. B., Mochrie, S. G. J. & Sutton, M. (2000). *Rev. Sci. Instrum.* **71**, 3274–3289.
Lurio, L. B., Lumma, D., Sandy, A. R., Borthwick, M. A., Falus, P., Mochrie, S. G. J., Pelletier, J. F., Sutton, M., Regan, L., Malik, A. & Stephenson, G. B. (2000). *Phys. Rev. Lett.* 84, 785–788.

Madsen, A., Als-Nielsen, J. & Grübel, G. (2003). *Phys. Rev. Lett.* **90**, 085701.
Madsen, A., Seydel, T., Sprung, M., Gutt, C., Tolan, M. & Grübel, G. (2004). *Phys. Rev. Lett.* **92**, 096104.
Marra, W. C., Eisenberger, P. & Cho, A. Y. (1979). *J. Appl. Phys.* **50**, 6927–6933.
Miao, J., Sayre, D. & Chapman, H. N. (1998). *J. Opt. Soc. Am. A*, **15**, 1662–1669.
Mochrie, S. G. J., Mayes, A. M., Sandy, A. R., Sutton, M., Brauer, S., Stephenson, G. B., Abernathy, D. L. & Grübel, G. (1997). *Phys. Rev. Lett.* **78**, 1275–1278.
Pfeiffer, F., Zhang, W. & Robinson, I. K. (2004). *Appl. Phys. Lett.* **84**, 1847–1849.
Philips, L. F. (2004). *J. Phys. Chem. B*, **108**, 1986–1991.
Robert, A., Wagner, J., Autenrieth, T., Härtl, W. & Grübel, G. (2005). *J. Chem. Phys.* **122**, 084701.
Robinson, I. K., Libbert, J. L., Vartanyants, I. A., Pitney, J. A., Smilgies, D. M., Abernathy, D. L. & Grübel, G. (1999). *Phys. Rev. B*, **60**, 9965–9972.
Robinson, I. K., Pindak, R., Fleming, R. M., Dierker, S. B., Ploog, K., Grübel, G., Abernathy, D. L. & Als-Nielsen, J. (1995). *Phys. Rev. B*, **52**, 9917–9924.
Seydel, T., Madsen, A., Sprung, M., Tolan, M.,Grübel, G. & Press, W. (2003). *Rev. Sci. Instrum.* **74**, 4033–4040.
Seydel, T., Madsen, A., Tolan, M., Grübel, G. & Press, W. (2001). *Phys. Rev. B*, **63**, 073409.
Seydel, T., Tolan, M., Ocko, B. M., Seeck, O. H., Weber, R., DiMasi, E. & Press, W. (2002). *Phys. Rev. B*, **65**, 184207.
Sikharulidze, I., Dolbnya, I. P., Fera, A., Madsen, A., Ostrovskii, B. I. & de Jeu, W. H. (2002). *Phys. Rev. Lett.* **88**, 115503.
Sikharulidze, I., Dolbnya, I. P., Madsen, A. & de Jeu, W. H. (2005). *Opt. Commun.* **247**, 111–124.
Sinha, S. K., Sirota, E. B., Garoff, S. & Stanley, H. B. (1988). *Phys. Rev. B*, **38**, 2297–2311.
Sinha, S. K., Tolan, M. & Gibaud, A. (1998). *Phys. Rev. B*, **57**, 2740–2758.
Snigirev, A., Kohn, V., Snigireva, I. & Lengeler, B. (1996). *Nature* (*London*), **384**, 49–51.
Sutton, M., Mochrie, S. G. J., Greytak, T., Nagler, S. E., Berman, L. E., Held, G. A. & Stephenson, G. B. (1991). *Nature* (*London*), **352**, 608–610.
Thurn-Albrecht, T., Zontone, F., Grübel, G., Steffen, W., Müller-Buschbaum, P. & Patkowski, A. (2003). *Phys. Rev. E*, **68**, 031407.
Tsui, O. K. C., Mochrie, S. G. J. & Berman, L. E. (1998). *J. Synchrotron Rad.* **5**, 30–36.
Vartanyants, I. A., Pitney, J. A., Libbert, J. L. & Robinson, I. K. (1997). *Phys. Rev. B*, **55**, 13193–13202.
Vineyard, G. H. (1982). *Phys. Rev. B*, **26**, 4146–4159.